Supplementary Information (SI) for Journal of Materials Chemistry C.

Supporting Information

Ferroelectric Memcapacitive Dynamics from Nanoseconds to Milliseconds for Bio-Inspired Neuromorphic Computing and Control

Sai Jiang[a,b,†,*], *Chaoran Wu*[a,†], *Jinrui Sun*[a], *Sihao Xu*[a], *Shen Li*[a], *Yijie Lai*[a], *Ning Wang*[a], *Huafei Guo*[a,*], *Jianhua Qiu*[a] *and Yun Li*[b,*]

[a]School of Integrated Circuits Industry, Wang Zheng School of Microelectronics, Changzhou University, Changzhou, Jiangsu 213164, P. R. China.

[b]National Laboratory of Solid-State Microstructures, School of Electronic Science and Engineering, Collaborative Innovation Center of Advanced Microstructures, Nanjing University, Nanjing, Jiangsu 210093, P. R. China.

Experimental section

Formulation of precursor and deposition of thin-film. Hafnium-zirconium oxide ($Hf_{0.5}Zr_{0.5}O_2$, HZO) thin films were prepared through a sol-gel spin-coating approach. Hafnium isopropoxide ($HfC_{12}H_{28}O_4$, Sigma-Aldrich, 99.9 %) and zirconium oxynitrate hydrate ($ZrO(NO_3)_2 \cdot xH_2O$, Alfa Aesar, 99.9 %) were dissolved in anhydrous 2-methoxyethanol to form a 0.2 M equimolar precursor solution under continuous stirring. Heavily doped p-type Si wafers were sequentially cleaned with acetone, isopropanol, and deionized water, followed by UV-ozone treatment. The precursor sol was spin-coated at 3000 rpm for 30 s, followed by a two-step annealing process. The as-coated films were first pyrolyzed at 350 °C (in air/40min) to remove residual solvent/organics and densify the gel network, and then crystallized by rapid thermal annealing at 600 °C (15 min) under vacuum. A control sample subjected only to the 350 °C pyrolysis step (without vacuum RTA) does not exhibit discernible HZO diffraction peaks, supporting the necessity of the subsequent crystallization anneal for forming the ferroelectric phase.

Characterization of HZO films. The chemical composition of the annealed HZO films was examined by X-ray photoelectron spectroscopy (XPS, Thermo Fisher ESCALAB Xi^+), showing only Hf^{4+}, Zr^{4+}, and O without detectable sub-oxides. The crystalline structure was analyzed by X-ray diffraction (XRD, Bruker D8 Advance), where reflections at ~30-32° confirmed orthorhombic/tetragonal phases with suppressed monoclinic contribution. Atomic force microscopy (AFM, Bruker Dimension Icon, tapping mode) revealed a smooth surface with nanometer-scale roughness. Local ferroelectric switching was validated by piezoresponse force microscopy (PFM, Asylum Research Cypher ES), displaying clear domain contrast and butterfly-shaped amplitude-voltage loops with ~±0.6 V coercive voltages. Macroscopic ferroelectric properties were further evaluated using the PUND method (Radiant Precision Premier II) under triangular sweeps of ±3 V at 1 kHz, yielding well-saturated polarization-voltage hysteresis loops.

Fabrication and characterization of mem-capacitor. Capacitor devices were fabricated by depositing Ni (5 nm)/Au (50 nm) top electrodes (rectangular pads, $\sim 5 \times 10^{-3}$ cm^2) on the HZO/Si films *via* thermal evaporation through a shadow mask, with the doped Si substrate serving as the bottom electrode. Ni was used as an adhesion layer to improve the mechanical robustness of the Au contact (e.g., for wire bonding) and electrode engineering can further tune interfacial screening in HZO[1–3], while electrode-dependent interfacial effects were not specifically optimized in this work. Chips were mounted on custom PCBs using EPO-TEK H20E silver epoxy, cured under vacuum to ensure uniform bonding, and Au wire bonding (WETEL WT-2310) was employed for electrical connection. Electrical tests were performed on a probe station using a source meter (Keithley 2612B) and a ferroelectric analyzer (Radiant Precision Premier II). Transient voltage responses to sub-μs pulses were characterized using a waveform generator (Tektronix AFG31000 Series) and a digital oscilloscope (Tektronix TBS 1000C Series). All measurements were conducted at room temperature in air.

Reservoir computing based on memcapacitive synapses. Reservoir computing was evaluated using both experimental HZO device data and fitted phenomenological models. Input signals, including ECG datasets and artificial pulse trains, were normalized to the device voltage window and multiplexed with binary masks. Device dynamics were modeled by a dual-channel relaxation framework, with parameters (τ_{0f}, τ_{0s}, γ_f, γ_s, P_s, k_q) obtained from transient current fitting. Reservoir states were simulated in Python and trained *via* ridge regression with a 70:30 train/test split and cross-validation. This workflow confirmed that HZO memcapacitors support short-term plasticity, temporal filtering, and nonlinear transformation essential for efficient RC.

Hardware reservoir mapping and robotic response control. Packaged HZO memcapacitors were integrated onto custom PCBs *via* Au wire bonding and interfaced with an STM32-based test system. Input voltages were generated by a DAC8568 and device outputs were captured in real time by an ADS1256, enabling direct hardware mapping into the reservoir framework. For robotic demonstrations, multi-pulse excitations were applied and device responses were evaluated against predefined thresholds: high outputs triggered strong actuation, intermediate values produced moderate responses, and low outputs yielded minimal motion. Feeding ECG signals and artificial spike trains confirmed stable input-output-action correspondence, demonstrating real-time temporal pattern recognition and adaptive motor control driven by memcapacitive reservoirs. When the stimulation condition changes, Th_1/Th_2 are re-calibrated based on the measured V_OUT distribution.

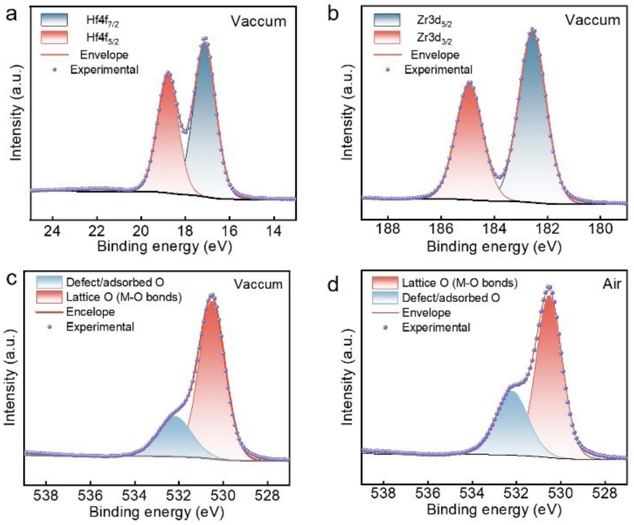

Figure S1. The XPS characterizations of HZO films. (a) Deconvolution of high-resolution Hf4f spectrum of RTA HZO thin film surface (vacuum). (b) Deconvolution of high-resolution Zr3d spectrum of RTA HZO thin film surface (vacuum). (c) Deconvolution of high-resolution O1s spectrum of RTA HZO thin film surface (vacuum). (d) Deconvolution of high-resolution O1s spectrum of RTA HZO thin film surface (air).

Vacuum RTA was performed in a low-pressure environment to reduce the oxygen partial pressure during crystallization, consistent with the main fabrication flow. An air-RTA control was annealed under the same temperature-time conditions in ambient atmosphere (higher oxygen chemical potential). Unless noted otherwise, all electrical/ferroelectric results in the main text are from vacuum-RTA devices, and the air-RTA sample is only used to benchmark the O1s chemistry.

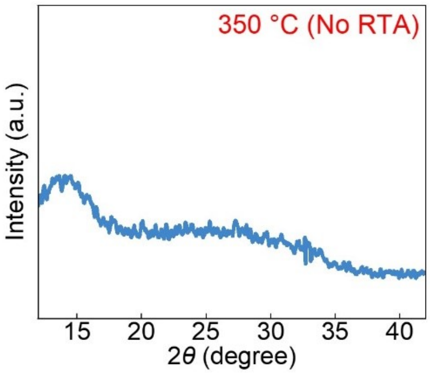

Figure S2. XRD patterns of sol-gel HZO films with and without vacuum RTA. The sample subjected only to the 350 °C air pyrolysis step exhibits no discernible HZO diffraction peaks, whereas the two-step annealed film (350 °C air + 600 °C vacuum RTA) shows the characteristic o-phase-related reflection near 2θ ≈ 30.5° (o-111), consistent with the main-text Fig.1e.

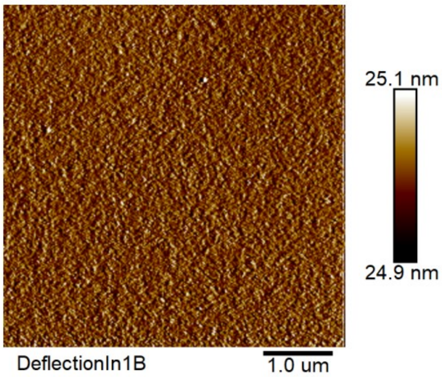

Figure S3. Atomic force microscope (AFM) height characterizations of Zr-doped HfO_2 (HZO) thin films.

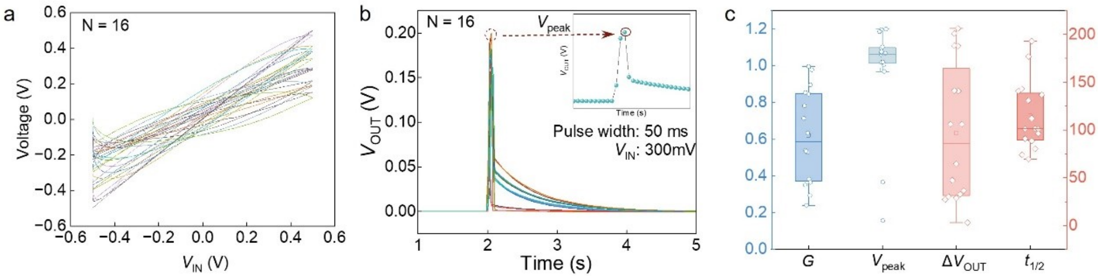

Figure S4. Device-to-device variability in a 4×4 array (N = 16). (a) Overlaid V_{IN}-V_{OUT} hysteresis loops measured within (-0.5, 0.5) V. (b) Overlaid EPSV transients under V_{IN} = 300mV. (c) Box plots of extracted metrics. For visualization, V_{peak} values are scaled by ×6 and $t_{1/2}$ values are scaled by ×5. All reported values and discussions refer to the original (unscaled) quantities. We note that 3-4 devices in the array exhibit weak or no obvious ferroelectric/synaptic signatures. The channels with clearly abnormal behavior are excluded in system demonstrations but remain included in the statistical analysis. Even with this level of device variability, the majority of devices retain finite hysteresis and synaptic responses within the same bias window, which is sufficient for the reservoir mapping used in this work.

To quantify the device-to-device spread in the practical operating region, we extracted the small-signal gain G by linearly fitting

$$V_{OUT} = GV_{IN} + b, V_{IN} \in [-0.3, 0.3]$$

At each V_{IN}, both the forward and backward sweep data points were included in the regression

$$G = \frac{\sum(x_i - \bar{x})(y_i - \bar{y})}{\sum(x_i - \bar{x})^2},$$

where $x_i = V_{IN}$ and $y_i = V_{OUT}$, so the fitted G represents an effective gain averaged over the two hysteresis branches and we defined the hysteresis opening width as

$$\Delta V_{OUT} = |V_{OUT-up}(0) - V_{OUT-down}(0)|,$$

where $V_{OUT\text{-}up}(0)$ is the value of the upper curve and $V_{OUT\text{-}down}(0)$ is the value in the opposite direction (right at V_{IN} = 0V). As summarized in Fig.R7c, the extracted values across the full array yield $G = 0.62 \pm 0.252$ (min-max: 0.240-0.996) and $\Delta V_{OUT} = 97.6 \pm 72.1$ mV (min-max: 3.1-206.4 mV). We note that the lower tail in ΔV_{OUT} is mainly associated with the aforementioned weak-ferroelectric devices, whereas the majority of devices retain a finite opening window within the same bias range.

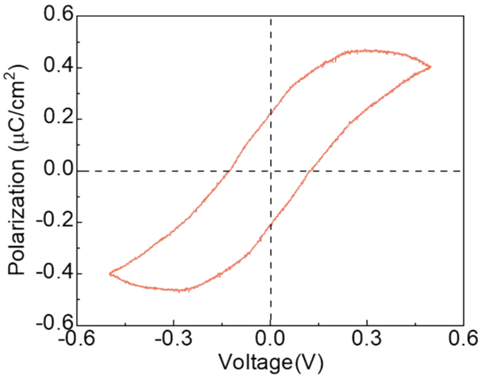

Figure S5.. Polarization hysteresis measured by the PUND method. P-V loops derived by integrating the transient response currents from the PUND. PUND suppresses the non-switching contributions (linear capacitive and leakage currents), and the extracted switching component evidences a non-negligible polarization-switching contribution in the HZO layer.

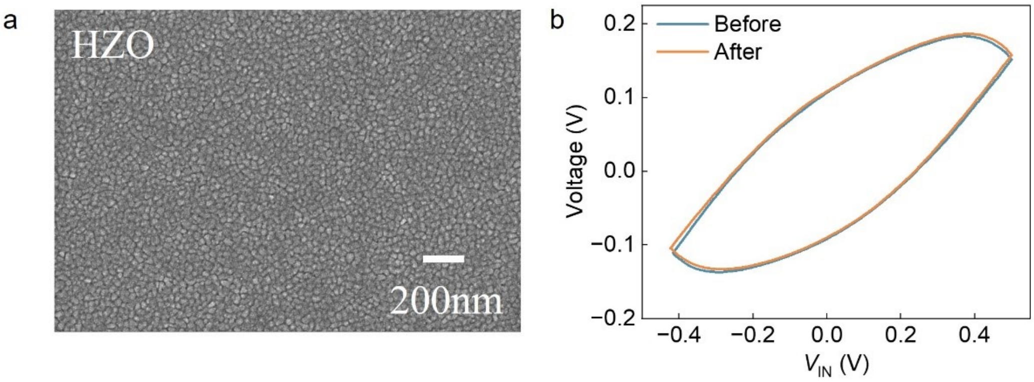

Figure S6. The structural stability of HZO. (a) Post-cycling SEM image of the HZO film after 10^3 electrical cycles. After cycling, the HZO film maintains a dense and crack-free morphology. (b) Ferroelectric hysteresis loops measured before and after 10^3 cycling in Au/Ni-electrode devices under a cycling window of -0.5 to 0.5 V. These results suggest that repeated electrical switching within the sub-volt operating window does not induce observable morphological damage or pronounced ferroelectric degradation, supporting the device robustness for subsequent system-level demonstrations.

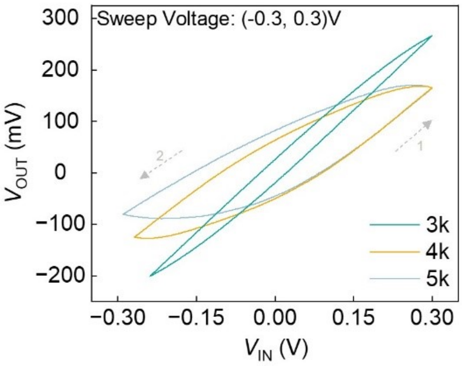

Figure S7. Polarization-voltage loops measured within ±0.3 V for HZO films prepared at 3000/4000/5000 rpm (lower thickness at higher spin speed). Ferroelectric hysteresis remains observable as the film is thinned, supporting the feasibility of further reducing the operating voltage by thickness scaling.

In this work, the 3000-rpm film (~20 nm) is used as the baseline. Although thinner films may enable lower-voltage switching, the 3000 rpm film provides a more stable hysteresis window and reproducible transient responses across devices, which is critical for reliable system-level demonstrations. The thickness-scaling data are included as supplementary evidence that lower-voltage operation is feasible, rather than to redefine the optimized thickness in the main text.

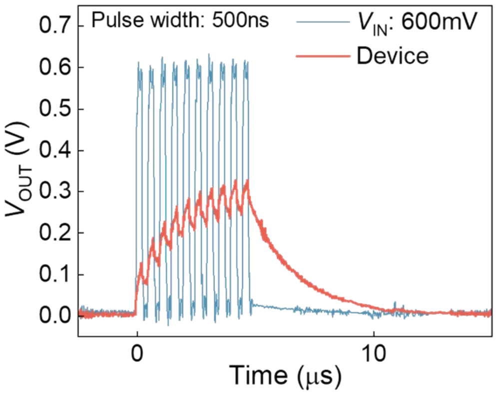

Figure S8. Representative multi-pulse response of the HZO memcapacitor to a 10-pulse train (V_{IN} = 600mV, pulse width = 500ns, 50% duty cycle). The input pulse train (blue) induces a cumulative V_{OUT} response (red) followed by a pronounced post-train relaxation tail back to baseline.

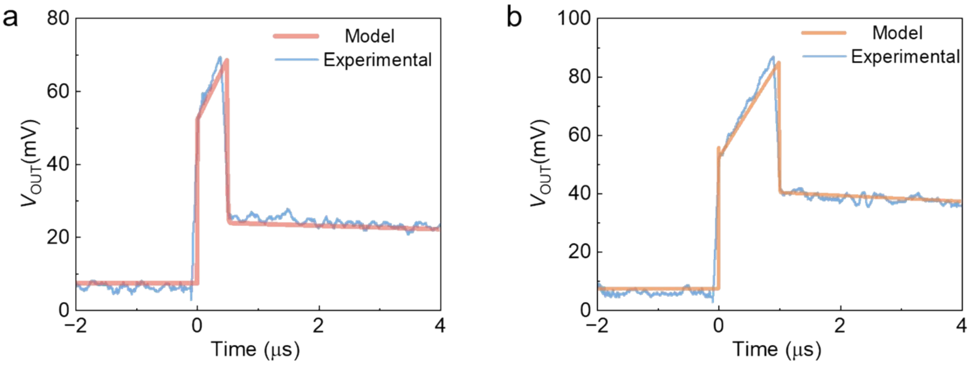

Figure S9. Experimental and fitted transient responses of HZO memcapacitive devices under sub-microsecond electrical pulses. (a) Response to a 500 ns input pulse. (b) Response to a 1 μs input pulse. Solid lines represent the experimental data, and dashed lines correspond to the results of the dual-relaxation polarization model coupled with an equivalent R-C which models the measurement-chain/parasitic loading and mainly affects the fastest transient component (**Note S2**). The optimized fitting parameters are summarized in Table S2.

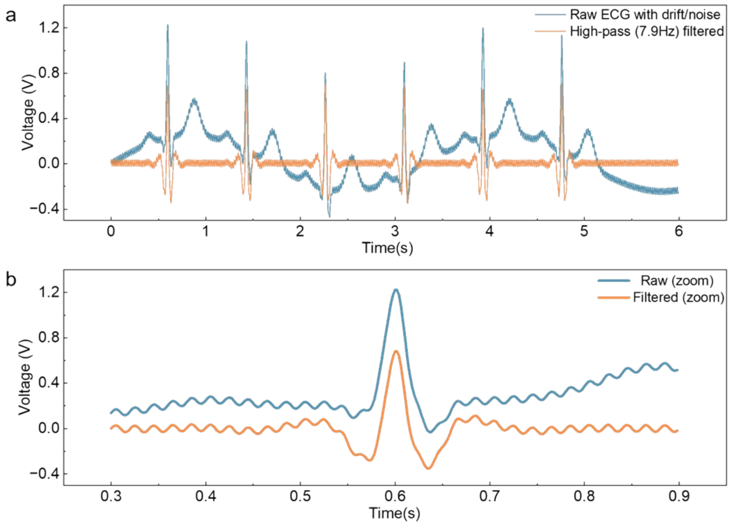

Figure S10. Demonstration of digital high-pass filtering of ECG signals with a cut-off frequency of 7.9 Hz. (a) Raw ECG with artificial low-frequency drift (blue) and the filtered output (orange), showing suppression of baseline wander. (b) Enlarged single beat illustrating that the P-QRS-T morphology is preserved after filtering.

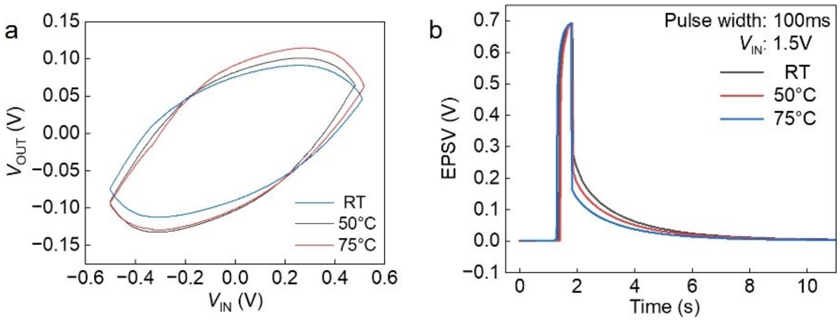

Figure S11. Temperature-dependent ferroelectric hysteresis and synaptic relaxation. (a) V_{IN}-V_{OUT} hysteresis loops measured at RT, 50 °C, and 75 °C. (b) EPSV decay traces at different temperatures under identical pulse conditions.

Peak	Area (P) (CPS·eV)	Sensitivity Factor (SF)	Corrected Area (A/SF)	Atomic %
C1s	52236.46	1	52236.46	11.22
Hf4f	461489.81	7.9	58416.43165	11.12
O1s	789324.76	2.881	273975.9667	67.5
Zr3d	448663.67	9.032	49674.89703	10.16

Table S1. XPS-derived atomic concentrations in the spin-coated HZO thin films.

Parameter	**Value**
β	3.47
α	8.11×10^{-2}
A	2×10^{-8}
τ_{0f}	4.72
τ_{0s}	6.03×10^{4}
γ_f	0.426
γ_s	0.872
ω_f	2.88×10^{-2}
k_q	1.14×10^{-3}
R_{leak}	4.25×10^{6}
C_{out}	4.26×10^{8}
V_{off}	7.39
P_s	0.635

Table S2. Parameters of equations uesd in sub-microsecond synaptic response simulation.

Neuromorphic hardware	**Operating Voltage(V)**	**Edurance cycles**	**Retention**	**Fabrication temperature**	**Classification accuracy / Data set**	***E***	**Ref.**
Pt/Ti/TiO_x/Al_2O_3/Pt/Ti	1.53/-1.65	2×10^5	10^4 s	N.A.	>98% / image	N.A.	4
Pt/Al/TiO_y/TiO_x/Al_2O_3/Pt	4/-1.5	10^2	10^4 s	450°C	95.03% / MNIST	L.P.C.	5
Pt/Al/TaO_x/Al_2O_3/SiO_2/AlN/Pt	1.5/-1.6	10^2	10^4 s	450°C	95.83% / MNIST	L.P.C.	6
Memristor crossbar array	1/-1	N.A.	N.A.	N.A.	95.47% / MNIST	3mJ$^{(1)}$	7
Ag/Ni-HfO_2/P^{++}-Si	2.5/-2.5	10^2	40 days	RT	N.A.	L.P.C.	8
TiN/GeSbTe/TiN	N.A.	> 1.1×10^{11}	10^9 cycles	N.A.	N.A.	N.A.	9
Ge-rich $Ge_2Sb_2Te_5$/Si	1.5 /1.8-2.7	N.A.	6×10^7s	28nm FD-SOI CMOS	71.7% / MNIST	N.A.	10
W/Ti/SbTe/W	0.6/-0.6	> 8.6×10^4	10^3s	200°C	88% / MNIST	N.A.	11
W/TiN/$Ge_2Sb_2Te_5$/Si_3N_4/W	2	10^5	10 years	180°C	N.A.	148pJ	12
TiN/Ti/Si:HfO_2/TiN	FeCAP: 3 Memristor: 1/4.5	FeCAP: >10^7 Memristor: ≈10^5	servral weeks	350°C	95.5% / ECG	< 200fJ	13
Ni/ITO/HZO/W/Al_2O_3/MICA	3.8/-2	>2×10^7	>10 years	400°C	91.8% / MNIST	L.P.C.	14
TiN/$HfZrO_2$/SiO_2/Si	5.5/-5	>10^7	10^6	650°C	96% / Chest X-ray	N.A.	15
Ni/MoS_2/Al_2O_3/W/HZO/SiO_2	4.9/-4.4	N.A.	>10^4	400°C	09% / MNIST	L.P.C.	16

Au/Ti/Al_2O_3 /HZO/TiN /SiO_2/Si	~5	>10^9	N.A.	600°C	N.A.	L.P.C	17
Ni/Ni/MoS_2/ $Hf_{0.25}Zr_{0.75}O_2$/ Al_2O_3/W	~5	>10^4	>10^3	500°C	95.6% / MNIST	L.P.C.	18
Au/Ni/ HZO/Si	**0.6/-0.6**	**10^3**	**10^3 s**	**600°C**	**97.7% physical, 99.7% model / ECG**	42fJ	**This work**

N.A.: not available

L.P.C.: low power consumption

(1) Total power consumption

Table S3. Quantitative benchmarking that compares the HZO-based memcapacitive system with other state-of-the-art neuromorphic hardware

Table S4 summarizes a literature benchmark of recent RRAM/PCM/FeFET neuromorphic devices. Because reported metrics are often obtained under different test protocols, we list the original operating conditions when available. The "working voltage" refers to the programming/switching voltage used in the cited work; the energy/power values are reported as stated in the references (device-only unless explicitly including peripheral circuits). This table is intended to contextualize the operating regime and system-level demonstration of our HZO memcapacitive reservoir rather than to claim a universal one-to-one comparison across all device platforms.

Note S1. The analysis of Hf: Zr composition ratio of $Hf_{1-x}Zr_xO_2$

In $Hf_{1-x}Zr_xO_2$, the Zr fraction plays a decisive role in balancing the phase competition among the monoclinic (m), orthorhombic (o), and tetragonal (t) polymorphs. To explicitly address the compositional comparison raised by the reviewer, we rely on established literature showing that the phase assemblage in $Hf_{1-x}Zr_xO_2$ evolves systematically with Zr fraction[19–21]. In general, Hf-rich compositions (lower x) tend to favor the thermodynamically stable monoclinic phase, which suppresses the polar orthorhombic (o) phase and weakens ferroelectricity, whereas increasing Zr content progressively reduces the monoclinic fraction and promotes o/t-phase mixtures[20–22]. Importantly, several studies further report that Zr-rich compositions can exhibit a transition toward tetragonal/antiferroelectric-like behavior, which competes with the polar o-phase and narrows the ferroelectric stability window at high x[22,23]. Consequently, compositions near x ≈ 0.5 typically provide a broader processing window where the polar orthorhombic phase fraction is maximized and remains more stable compared with Hf-rich or Zr-rich ratios[19,21–23].

In our study, the film composition is experimentally verified to be near-equimolar by XPS (Fig.S1 and Table S1). Specifically, the cation atomic concentration extracted from XPS follows the standard sensitivity-factor correction,

$$C_i \propto \frac{A_i}{SF_i}$$

where A_i is the background-corrected integrated peak area and SF_i is the instrumental sensitivity factor for element *i*. Accordingly, the Hf-to-Zr cation ratio can be written as

$$\frac{C_{Hf}}{C_{Zr}} = \frac{A_{Hf}/SF_{Hf}}{A_{Zr}/SF_{Zr}}$$

Using the values in Table S1 ($A_{\mathrm{Hf4f}} = 461489.81$, $SF_{\mathrm{Hf4f}} = 7.9$, $A_{\mathrm{Zr3d}} = 448663.67$, and $SF_{\mathrm{Zr3d}} = 9.032$), we obtain sensitivity-factor-corrected areas of $A/SF = 58416.43$ for Hf and 49674.90 for Zr, yielding Hf: Zr ≈ 1.18: 1. In addition, the atomic percentages reported by the XPS quantification software (11.12 % for Hf and 10.16 % for Zr) provide an independent estimate

$$Hf{:}Zr \approx \frac{atomic_{Hf}}{atmoic_{Zr}} = \frac{11.12}{10.16} \approx 1.09{:}1$$

which is closer to unity. Considering the typical uncertainty of quantitative XPS (on the order of ~ ±0.5-1 % per element), both calculations consistently indicate that the HZO film is effectively near-equimolar (Hf: Zr ≈ 1:1), corresponding to x ≈ 0.5.

Consistent with this composition, XRD (Fig.1e) exhibits a prominent o-phase signature (e.g., the o-111 reflection near ~30.5°) with suppressed monoclinic-related features, indicating that under our sol-gel processing and annealing conditions, a near-equimolar Hf: Zr ratio contributes to promoting and stabilizing the orthorhombic phase. Taken together, the literature-established composition–phase relationship and our direct compositional verification (Fig.S1 and Table S1) support the view that the selected Hf: Zr ratio helps enable robust formation and retention of the o-phase in our films.

Note S2. Modeling and Fitting of Transient Output Dynamics in HZO Devices

To quantitatively describe the transient response of HZO-based memcapacitive devices under sub-microsecond voltage pulses, we established a physical fitting model that combines nonlinear ferroelectric polarization dynamics with an equivalent R-C representation of the measurement-chain/parasitic loading (Fig.S9). This equivalent R-C representation does not correspond to a physically implemented readout circuit but only captures the parasitic loading of the measurement chain.

The polarization dynamics were derived from a Landau-Khalatnikov-type approach, assuming that the system tends to relax toward a nonlinear equilibrium polarization P_∞. When the input is a rectangular pulse with amplitude V_{IN} and pulse width T_{pw}:

$$V = V(t) = \begin{cases} V_{IN}, & 0 \leq t < T_{pw} \\ 0, & \text{otherwise} \end{cases}$$

, the measured output is the middle-node voltage of the device operating as two series capacitors, only a fraction of the applied voltage drops on the ferroelectric layer; we thus define the internal field across HZO as

$$E = \frac{\eta V_{IN}}{d_{fe}}, \ \eta = \frac{1}{2} \tag{S1}$$

The nonlinear static endpoint toward which the polarization relaxes is taken from the phenomenological equilibrium relation used in **Note S6**, now written explicitly as

$$P_\infty(E;P') \equiv P_{eq}(E;P') = P_s \tanh\left[\beta(E + \alpha P')\right], \ \beta = \frac{p}{k_B T} \tag{S2}$$

where P_s is the saturation polarization (equivalently $P_s = np$, n is the dipoles density, p is the effective dipole moment) , $k_B T$ the thermal energy, and $\alpha P'$ provides the mean-field (Weiss) feedback from a history/slow variable P'. In the transient model below we identify the target as $P_\infty(E;\, P')$ and approximate P' by the slow-channel polarization (i.e., $P'(t) \approx P_2(t)$), which preserves the hysteresis-bearing “memory”.

The polarization is decomposed into a fast channel P_1 and a slow channel P_2, both relaxing toward the same endpoint P_∞:

$$P_1(t) = \frac{dP_1}{dt} = \frac{P_\infty(E;P_2) - P_1}{\tau_f(E)}, \ P_2(t) = \frac{dP_2}{dt} = \frac{P_\infty(E;P_2) - P_2}{\tau_s(E)} \tag{S3}$$

and the observable polarization is their weighted superposition

$$P(t) = \frac{dP}{dt} = \omega_f P_1(t) + (1 - \omega_f) P_2(t), \quad 0 \le \omega_f \le 1. \tag{S4}$$

The slow channel P_2 is introduced to capture the non ideal relaxation processes that become prominent under sub coercive excitation, such as slow interfacial screening equilibration and trap related relaxation, which give rise to the relaxation tail in the measured EPSV waveforms.

Field-dependent characteristic times follow a thermally assisted, field-accelerated (Merz/Arrhenius-like) form

$$\tau_{f,s}(E) = \tau_{f,s}^{0} exp\left[\frac{\Delta G_{f,s} - \mu_{f,s} pE}{k_B T}\right] = \hat{\tau}_{f,s} exp\left[-\gamma_{f,s}\frac{\eta V_{IN}}{d_{fe}}\right] \tag{S5}$$

$$\hat{\tau}_{f,s} \equiv \left[\tau_{f,s}^{0} \exp\left(\frac{\Delta G_{f,s}}{k_B T}\right)\right], \quad \gamma_{f,s} \equiv \mu_{f,s} p/(kBT)$$

where $\tau_{0f,s}$ denotes the intrinsic time constants of the fast and slow channels, $\gamma_{f,s}$ describes their sensitivity to the applied voltage amplitude. Besides, $\Delta G_{f,s}$ is the effective barriers, and $\mu_{f,s}$ is the geometric/domain-kinetic coefficients. It is noted that the $\Delta G/k_B T$ term is been absorbed into $\tau_{0f,s}$ for the sake of avoidance of the complexity of model fitting parameters. This parameterization makes explicit how thinner films (smaller d_{fe}) or larger V_{IN} accelerate the dynamics through a larger internal field E.

The transient output voltage is then determined by an equivalent RC balance between capacitive charging and polarization current injection:

$$C_{out}\frac{dV_{out}}{dt} + \frac{V_{out}}{R_{leak}} =- A\frac{dP}{dt} \tag{S6}$$

Here, R_{leak} is the equivalent discharge resistance, C_{out} denotes the equivalent output capacitance (including parasitics), and A is the effective electrode area. These R_{leak} and C_{out} terms represent lumped measurement-chain/parasitic loading at the V_{OUT} node rather than an intentionally implemented external readout circuit. The corresponding $\tau_{R\text{-}C} = R_{leak}C_{out}$ mainly shapes the fastest transient component rather than the long relaxation tail. Finally, the measured signal is reported as:

$$V_{OUT}(t) = k_q V_{out}(t) + V_{off},\ k_q = \frac{A}{C_{out}} \times \text{(gain/unit conversion)} \tag{S7}$$

with V_{off} compensating baseline offsets and k_q standing for a coupling constant that converts the polarization rate into an observable voltage signal. The V_{out} denotes the internal node voltage of the equivalent RC model (V), while V_{OUT} corresponds to the experimentally observed signal after unit conversion and offset correction (mV). Equations (S3)-(S7) are integrated directly on the experimental (generally non-uniform) time grid using a forward-Euler scheme. Denoting the state vector by $X = (P_1, P_2, V_{\mathrm{out}})$ and $\Delta t_i = t_{i+1} - t_i$, the update reads

$$X_{i+1} = X_i + \Delta t_i \cdot \frac{dX}{dt}|_{t_i}, \ \Delta t_i > 0 \tag{S8}$$

while for duplicate/non-increasing stamps the state is held to ensure stability and to respect the acquisition sequence,

$$X_{i+1} = X_i, \ \Delta t_i \le 0 \tag{S9}$$

Non-uniform sampling intervals in the experimental dataset were handled naturally by using the actual Δt_i. In the case of duplicate or non-increasing time stamps, the system state was held constant in (Eq.S9). This approach ensures numerical stability and accurate reproduction of the measured transient waveforms across both sub-µs and µs excitation timescales.

The initial conditions were set as $P_1(0) = P_2(0) = V_{\mathrm{out}}(0) = 0$. The complete parameter set $\{\tau_{0f,s}, \gamma_{f,s}, \omega_f, A, C_{\mathrm{out}}, R_{\mathrm{leak}}, k_q, V_{\mathrm{off}}, P_{\mathrm{s}}, \alpha\}$ was optimized using least-squares fitting to experimental waveforms at different pulse widths (Table S2). With $E = \eta V_{\mathrm{IN}}/d_{\mathrm{fe}}$ ($\eta = 1/2$) and the identification $P_\infty \equiv P_{\mathrm{eq}}$ from Note S4 in Eq.(S1), this dual-relaxation framework consistently reproduces the sharp rising edges and slower relaxation tails of sub-µs transients (main text, Fig.2b) while remaining compatible with the quasi-static hysteresis-like behavior (main text, Fig.2g), thereby unifying transient and steady responses within one physically consistent picture. In this sense, the slow component in the transient model plays a role analogous to the effective relaxation factor in the quasi static mapping, because both account for sub-coercive non ideal relaxation that is not governed by instantaneous polarization reversal. In a physical sense, the fast channel is consistent with a polarization-related rapid response under pulsed excitation, whereas the slow channel may reflect depolarization-associated screening-charge redistribution and/or trap-assisted relaxation coupled to polarization, which can modulate the fading-memory time constants.

Note S3. Paired-Pulse Facilitation (PPF) of HZO thin film memcapacitive synapses

To investigate the short-term synaptic plasticity, PPF behavior was simulated in the HZO memcapacitive synapses. Two consecutive pre-synaptic voltage pulses (T_{width} = 50 ms) were applied to the input terminal, and the corresponding EPSV responses were recorded. As shown in the main panel, the second EPSV (A_2) exhibits a larger amplitude than the first EPSV (A_1), confirming a facilitation effect analogous to biological synapses.

The PPF index is defined as the ratio of the second to the first EPSV (A_2/A_1), and its dependence on the interpulse interval Δt can be fitted by a double exponential decay function:

$$PPF(\Delta t) = 1 + C_1 e^{-\Delta t/\tau_1} + C_2 e^{-\Delta t/\tau_2} \tag{S10}$$

where τ_1 and τ_2 are the characteristic relaxation times of the fast and slow processes, respectively, while C_1 and C_2 represent the initial facilitation strengths. From the fitting, we obtained $C_1 = 0.12128$, $C_2 = 0.12705$, $\tau_1 = 47$ μs, and $\tau_2 = 609$ μs. These results reveal that the HZO memcapacitive synapses exhibit a coexistence of rapid and persistent relaxation dynamics, enabling nonlinear, time-dependent voltage responses. Such behavior closely emulates biological paired-pulse facilitation and provides a functional basis for temporal information encoding in reservoir computing systems.

Note S4. Frequency-dependent gain fitting of HZO memcapacitive synapses

To quantitatively describe the frequency-dependent facilitation behavior of HZO memcapacitive devices (main text, Figure 2f), we analyzed the EPSV gain under repetitive pulse stimulation. The gain is defined as the ratio between the response amplitude of the tenth pulse and that of the first pulse,

$$Gain = \frac{A_{10}}{A_1}$$

As the input pulse frequency increases, the gain exhibits a monotonic enhancement, which reflects the intrinsic high-pass filtering characteristics of the device. The experimental data were fitted with a phenomenological high-pass filter function:

$$H(f) = 1 - exp\left(-\frac{f^2}{2f_H^2}\right)$$

where f is the pulse frequency and f_H denotes the cut-off frequency. The obtained cut-off frequency ($f_H \approx 7.9$ Hz) corresponds to the characteristic transition point above which high-frequency inputs are selectively transmitted, while low-frequency components are strongly attenuated. This fitting framework provides a simple and robust description of the frequency-dependent synaptic gain and establishes a direct analogy to biological synapses acting as high-pass filters.

Note S5. Temperature as a parameter affecting polarization response and relaxation kinetics

To clarify the physical meaning of the temperature parameter T in Eq.1, we performed temperature-dependent measurements at room temperature (RT), 50 °C, and 75 °C under identical electrical stimulation conditions (pulse amplitude/width/interval kept the same). Figure S11 summarizes both the ferroelectric hysteresis behavior and the synaptic relaxation dynamics at these temperatures. The hysteresis remains observable across the tested temperature range, indicating that the polarization switching contribution is preserved, while the loop becomes noisier at elevated temperature, which is consistent with thermally activated screening/charge dynamics in oxide ferroelectrics.

For a fair comparison of relaxation kinetics, the EPSV decay traces are normalized by the peak response

$$A_{norm}(t) = \frac{EPSV(t)}{EPSV_{max}},$$

where $\mathrm{EPSV_{max}}$ is the maximum EPSV immediately after the stimulus at the same temperature. After normalization, the residual amplitude decreases monotonically with temperature (e.g., evaluated at t = 0.1s: 0.354 at RT, 0.296 at 50 °C, and 0.217 at 75 °C), indicating accelerated relaxation kinetics and a shortened fading-memory window at higher temperature. These results support treating T as a key parameter that modulates both the polarization-related response and the relaxation/screening processes in the device, consistent with the model interpretation in the main text.

Note S6. Derivation of the phenomenological model

To analytically describe the nonlinear polarization-output relation used in the main text, we adopted a mean-field approximation similar to prior reports. Within the Weiss mean-field framework, the local electric field experienced by dipoles can be expressed as

$$E_{loc} = E_{IN} + \alpha P \tag{S11}$$

where E_{IN} is the externally applied field, P is the polarization, and α is a feedback coefficient representing dipole-dipole interactions. Moreover, $\alpha \cdot P$ is the Weiss field evoked by the polarization P. There are two capacitors in series in the equivalent circuit:

$$E_{IN} = \frac{V_{IN}}{2d_{fe}} \tag{S12}$$

The equilibrium (static) polarization follows the Weiss-type mean field with the Langevin tanh approximation (notation as in the main text and **Note S2**)::

$$P_{eq}(E;P^{'}) = P_s \tanh\left(\frac{p(E_{IN} + \alpha P^{'})}{k_B T}\right) \tag{S13}$$

where the polarization P_{eq} is combined with dipoles' density (n) and dipolar moment (p) to the applied bias E_{IN}, scaled by the Boltzmann constant (k_{B}), thermal activation (T), and dielectric thickness (d_{fe}) of HZO. While $k_{\mathrm{B}}T$ is the thermal energy and the additional $\alpha P'$ term accounts for history-dependent polarization, thereby embodying the intrinsic hysteresis of ferroelectric systems. In practice under slow scans we may take $P'(t) \approx P(t - \Delta t)$ (one-step memory). For cross-consistency with **Note S2**, one can also set $P'(t) \approx P_2(t)$ (the slow channel in the dual-relaxation model).

Assuming first-order kinetics toward the equilibrium curve above, the quasi-static polarization follows

$$\frac{dP}{dt} = -\frac{P - P_{eq}(E;P^{'})}{\tau_{sys}} \tag{S14}$$

with a single phenomenological time constant τ_{sys}. This is the slow-scan counterpart of **Note S2**, where the same relaxation is later resolved into field-dependent fast/slow channels.

For a time step Δt_i at (approximately) fixed E_i and P_i', (S14) admits the exact step solution

$$P_{i+1} = P_{eq}(E_i; P_i')\left(1 - e^{-\Delta t_i/\tau_{sys}}\right) + P_i e^{-\Delta t_i/\tau_{sys}} \tag{S15}$$

It is convenient to identify the relaxation factor as a derived quantity,

$$k_t(\Delta t_i) \equiv 1 - e^{-\Delta t_i/\tau_{sys}} \tag{S16}$$

so that $P_{i+1}=(1-k_t)P_i + k_t P_{\mathrm{eq}}$. Hence k_t is uniquely determined by τ_{sys} and the scan dwell time Δt_i. Its complementary keep fraction is $\exp(-\Delta t_i/\tau_{\mathrm{sys}})$. In this quasi-static description, k_t quantifies the degree to which the polarization approaches equilibrium within each dwell step. Under sub-coercive excitation, slow screening/trap-assisted relaxation is not treated as a parasitic error term but is quantitatively absorbed into k_t through τ_{sys} and the dwell time Δt_i, thereby shaping the apparent quasi-static hysteresis.

When time derivatives vanish on average over a quasi-static step, the measured voltage is well described by a linear mapping of the input and the instantaneous polarization

$$V_{OUT} = k_1 V_{IN} + k_2 P(t) + V_{off} \tag{S17}$$

Here k_1 captures the effective capacitive division/readout gain, k_2 converts polarization to voltage, and V_{off} is a baseline offset. This corresponds to Equation (2) in the main text. The quasi-static model assumes stationary parameters over the measurement window. Therefore, although the present model assumes time-invariant parameters over the calibration window, it can be extended to explicitly include aging by introducing an aging-time variable t_a and allowing the key parameters to evolve slowly with t_a, namely $P_s(t_a)$, $\alpha(t_a)$, $\tau_{\mathrm{sys}}(t_a)$, $k_2(t_a)$, and $V_{\mathrm{off}}(t_a)$, while keeping the governing equations and the numerical update structure unchanged.

For consistency with the transient model, the static endpoint used there is identified with the equilibrium relation here, $P_\infty(E; P') \equiv P_{\mathrm{eq}}(E; P')$. The single time scale τ_{sys} that governs slow scans is resolved in the transient framework into field-assisted fast/slow channels to capture sub-μs dynamics, while both descriptions share the same field definition $E = \eta V_{\mathrm{IN}}/d_{\mathrm{fe}}$ and the same endpoint P_{eq}, ensuring parameter-level coherence across figures.

The phenomenological model described in Equation (S11)-(S17) was employed to reproduce the quasi-static hysteresis-like characteristics of the HZO memcapacitor, as shown in Figure 2g of the main text. With the initial polarization state set to $P' = -0.5$ and empirical parameters chosen as $k_1 = 0.1$ and $k_2 = 11$, the calculated V_{OUT} closely follows the experimental curves, capturing both the nonlinear switching behavior and the gradual relaxation dynamics.

Note S7. Rationale for choosing M = 50 and mask definition

In this work, the temporal mask length is set to M = 50, which is a commonly adopted choice in prior reservoir-computing demonstrations and provides sufficient virtual-node dimensionality for ECG feature projection. The mask matrix is bipolar with entries in [-1, 1], which is converted into a sequence of M pulses for hardware mapping. Considering the system-level time budget, the pulse width is set to 10 ms (50 % duty), so the mapping latency per ECG segment is ~M × 10 = 500 ms, remaining within an acceptable range for our real-time demonstration. Fig.3g, h summarizes the training convergence and the confusion matrix obtained with M = 50, supporting that this choice provides a good accuracy-latency trade-off in our setup.

Note S8. Robustness to device non-idealities and drift in training/inference

In our workflow, the readout is trained using reservoir states obtained from device-mapped responses (or an empirically calibrated model constrained by device measurements), rather than from idealized, noise-free signals. Therefore, the training set already contains non-idealities such as response dispersion, baseline fluctuation, and relaxation-related variability, which acts as an implicit augmentation and improves robustness against moderate drift. In addition, the fully connected classifier reaches 97.7 % accuracy without explicit noise injection. Given the hardware-derived nature of the state representation and the five-class ECG task, this accuracy level is sufficient for the demonstrated signal-to-action pipeline. If needed, long-term drift can be further mitigated by lightweight periodic recalibration (e.g., baseline normalization) or re-fitting the linear readout with a small set of updated samples. In addition, the electrical cycling test in Fig.S6 indicates that the device structure and ferroelectric response remain stable over repeated switching within the operating window.

References

1 T. K. Paul, A. K. Saha and S. K. Gupta, *J. Appl. Phys.*, 2025, **137**, 144102.

2 A. G. Chernikova, M. G. Kozodaev, R. R. Khakimov, S. N. Polyakov and A. M. Markeev, *Appl. Phys. Lett.*, 2020, **117**, 192902.

3 V. V. Afanas'ev, A. Stesmans, L. Pantisano, S. Cimino, C. Adelmann, L. Goux, Y. Y. Chen, J. A. Kittl, D. Wouters and M. Jurczak, *Appl. Phys. Lett.*, 2011, **98**, 132901.

4 T.-H. Kim, S. Kim, J. Park, S. Youn and H. Kim, *ACS Appl. Electron. Mater.*, 2024, **6**, 4099–4107.

5 M. Noh, D. Ju and S. Kim, *J. Mater. Chem. C*, 2024, **12**, 13516–13524.

6 M. Noh and S. Kim, *J. Mater. Chem. C*, 2025, **13**, 20675–20689.

7 M. Bettayeb, Y. Halawani, M. U. Khan, H. Saleh and B. Mohammad, *Sci Rep*, 2024, **14**, 24173.

8 R. Khan, S. Iqbal, K. N. Hui, E. A. Khera, S. Kalluri, M. Soliyeva and S. Sangaraju, *Sensors and Actuators A: Physical*, 2025, **385**, 116316.

9 J. Zheng, R. Wang, W. Fang, C. Li, J. Zhang, Z. Wan, Y. Chen, J. Liu, X. Zou, L. Xie, Q. Wang, X. Li, S. Song, X. Zhou and Z. Song, *Nat Commun*, 2025, **16**, 5788.

10 J. H. Quintino Palhares, N. Garg, P.-A. Mouny, Y. Beilliard, J. Sandrini, F. Arnaud, L. Anghel, F. Alibart, D. Drouin and P. Galy, *npj Unconv. Comput.*, 2024, **1**, 8.

11 J. S. Oh, H. J. Lee, J. Y. Choi, K. A. Nirmal, D. H. Kim, J. M. Joo, T. D. Dongale and T. G. Kim, *Small*, **n/a**, e14024.

12 N. Hur, Y. Kim, B. Park, S. Yoon, S. Kim, D.-H. Lim, H. Jeong, Y. Kwon and J. Suh, *Small Methods*, 2025, **9**, 2401381.

13 M. Martemucci, F. Rummens, Y. Malot, T. Hirtzlin, O. Guille, S. Martin, C. Carabasse, A. F. Vincent, S. Saïghi, L. Grenouillet, D. Querlioz and E. Vianello, *Nat Electron*, 2025, **8**, 921–933.

14 Q. Li, S. Wang, Z. Li, X. Hu, Y. Liu, J. Yu, Y. Yang, T. Wang, J. Meng, Q. Sun, D. W. Zhang and L. Chen, *Nat Commun*, 2024, **15**, 2686.

15 M. Song, R.-H. Koo, J. Kim, C.-H. Han, J. Yim, J. Ko, S. Yoo, D. Choe, S. Kim, W. Shin and D. Kwon, *Nat Commun*, 2025, **16**, 6879.

16 H. Xiang, L. Li, Y.-C. Chien, H. Zheng, J. Gao and K.-W. Ang, *ACS Appl. Mater. Interfaces*, 2025, **17**, 32575–32585.

17 X. Li, P. Srivari, E. Paasio and S. Majumdar, *Nanoscale*, 2025, **17**, 6058–6071.

18 Y. Shi, Z. Zheng, J. Huo, Y.-C. Chien, S. Li, H. Zheng, X. Gong and K.-W. Ang, *Nano-Micro Lett.*, 2026, **18**, 202.

19 T. Song, H. Tan, N. Dix, R. Moalla, J. Lyu, G. Saint-Girons, R. Bachelet, F. Sánchez and I. Fina, *ACS Appl. Electron. Mater.*, 2021, **3**, 2106–2113.

20 H. A. Hsain, Y. Lee, G. Parsons and J. L. Jones, *Appl. Phys. Lett.*, 2020, **116**, 192901.

21 S. W. Smith, A. R. Kitahara, M. A. Rodriguez, M. D. Henry, M. T. Brumbach and J. F. Ihlefeld, *Appl. Phys. Lett.*, DOI:10.1063/1.4976519.

22 S. S. Fields, D. H. Olson, S. T. Jaszewski, C. M. Fancher, S. W. Smith, D. A. Dickie, G. Esteves, M. D. Henry, P. S. Davids, P. E. Hopkins and J. F. Ihlefeld, *Appl. Phys. Lett.*, 2021, **118**, 102901.

23 H. Dahlberg, A. E. O. Persson, R. Athle and L.-E. Wernersson, *ACS Appl. Electron. Mater.*, 2022, **4**, 6357–6363.